A Water Mass Model of the World Ocean

K. Bryan and L. J. Lewis

Geophysical Fluid Dynamics Laboratory/NOAA, Princeton University, Princeton, New Jersey 08540

A numerical model of the world ocean is developed to investigate the role of the ocean in the earth's heat balance. Climatological wind stress, temperature, and salinity are imposed as upper boundary conditions. An equilibrium solution is obtained based on an extended numerical integration over the equivalent of 1000 years. Seasonal variations are included. A series of numerical integrations over shorter periods indicate that quantitative aspects, such as the scale depth of the thermocline, are very sensitive to the closure parameterization representing the effect of unresolved scales of motion. The mean depth of the thermocline is found to be in proportion to the global available potential energy. Larger wind driving increases the scale depth of the thermocline, while larger lateral friction or diffusion leads to a shallower thermocline. The model predicts three major meridional cells in the upper thermocline in each hemisphere, corresponding to the three meridional cells of the atmosphere. The tropical and mid-latitude cells are largely wind driven. Thermohaline effects are dominant in the polar meridional cells. Seasonal changes in winds have a profound effect on the meridional circulation in the tropics and cause a flux of surface water from the summer to the winter hemisphere. It is suggested that this mechanism is an important factor in moderating climate by transferring excess heat from the summer hemisphere into the winter hemisphere.

1. Introduction

The ocean's role in the global heat balance and climate is universally recognized, but as yet little is known of the details of the transfer of heat by the world ocean. On time scales much longer than 1 year the entire global ocean circulation must be considered. This view is quite unfamiliar to many modern physical oceanographers but is quite in keeping with classical oceanography. The description and classification of large-scale water masses was the major activity of oceanography in its earlier phases. Geochemistry has provided new data over the last few decades, which have added important quantitative detail to earlier studies. Radioactive tracers have provided estimates of the average turnover time of deep water, for example. The study of water masses is closely related to climate through the global balance of heat and moisture. Quantitative models are needed to bring together the many indirect lines of evidence available to us in the field data.

The present study has been briefly described by *Bryan* [1979] in a volume that is concerned with a whole hierarchy of models that are being developed to study the ocean circulation. These formulations range from very simple tracer models intended to study the geochemistry of the deep sea (see *Veronis* [1977] for a review) to very detailed, eddy-resolving models of the ocean circulation (see *Holland* [1977] for a review). Some very interesting two-layer world ocean models have been developed by *Andreyev et al.* [1976] and by *Veronis* [1973, 1976]. The present model is being developed to be used in climate studies with a numerical model of the atmospheric circulation. To meet the requirements for studying the global heat balance, however, some compromise must be made in the horizontal resolution. The effect of mesoscale motions must be taken into account implicitly by approximate closure schemes. The formulation of closure schemes to represent the effects of mesoscale eddies and smaller-scale turbulence in the ocean based on the examination of field data and eddy-resolving models is an active area of research. Unfortunately, only preliminary results are available, so at present we must be satisfied with somewhat ad hoc schemes which really cannot be justified on the basis of field evidence. The alternative of an explicit eddy-resolving model

of the world ocean is not really available to us. A rough estimate indicates that such a model would require 3 orders of magnitude more computer time than is being used in the present study.

The present model is similar in many respects to that used in the combined ocean-atmosphere model by *Manabe et al.* [1975] and *Bryan et al.* [1975]. In those studies the climate equilibrium corresponding to a solar insolation without seasonal effects was determined by solving an initial value problem. From the solutions it was somewhat difficult to evaluate the effectiveness of the ocean model, since the boundary conditions that evolved at the ocean surface were quite different from those actually observed. The purpose of the present study is to examine the properties of the ocean model in isolation by driving the model with known climatological boundary conditions at the upper surface. In this way a fair comparison of the solutions can be made with respect to subsurface data on water mass properties and deep western boundary currents. The first part of this study is the analysis of a series of numerical experiments in which the closure parameters are systematically varied. The sensitivity of the system is measured by overall energy integrals. The second part is a detailed analysis of the mechanisms of poleward heat transport in the model.

2. Equations of the Model

Let $\mathbf{u}(\lambda, \theta, z, t)$ be a vector representing the independent variables of the model, such as velocity, temperature, and salinity. It is always possible to divide $\mathbf{u}$ into two components, $\mathbf{u} = \bar{\mathbf{u}} + \mathbf{u}'$, where $\bar{\mathbf{u}}$ represents the most probable state of the ocean for a given set of boundary and initial conditions and $\mathbf{u}'$ is the deviation from $\bar{\mathbf{u}}$. The equations of the model are written as predictive equations for $\bar{\mathbf{u}}$, and the effects of $\mathbf{u}'$ are introduced through closure approximations.

For large-scale motions in the ocean it is appropriate to simplify the equations of motion by introducing the hydrostatic approximation and the Boussinesq approximation. Let $\mathbf{v}$ be a horizontal velocity vector and w the vertical component. If ∇ is the horizontal gradient operator,

$$\partial_t \mathbf{v} + \mathbf{v} \cdot \nabla \mathbf{v} + w \partial_z \mathbf{v} + (2\Omega + \lambda) \sin \phi k \times \mathbf{v} =$$
$$-\rho_0^{-1} \nabla p + A_{MV} \partial_z \partial_z \mathbf{v} + \mathbf{F} \qquad (1)$$

$$\rho g = -\partial_z p \qquad (2)$$

TABLE 1. Resolution, Diffusivity, and Viscosity Coefficients for Experiments I–XIII

Experiment	$\Delta\lambda, \Delta\phi$, rad	(A_S, A_B), $\times 10^3$ ms^{-1}	(η_S, η_B), $\times 10^{-4}$ m^2 s^{-1}	A_{MH}, $\times 10^6$ m^2 s^{-1}	Remarks
I	$2\pi/64, \pi/38$	(2.5, 0.5)	(0.3, 1.3)	8	annual boundary condition
II	$2\pi/64, \pi/38$	(2.5, 0.5)	(0.3, 1.3)	8	seasonal boundary condition
III	$2\pi/128, \pi/76$	(1.0, 0.5)	(0.3, 1.3)	1	high resolution
IV	$2\pi/64, \pi/38$	(2.5, 0.5)	(0.3, 1.3)	4	low A_{MH}
V	$2\pi/64, \pi/38$	(2.5, 0.5)	(0.3, 1.3)	16	high A_{MH}
VII	$2\pi/64, \pi/38$	(1.0, 0.5)	(0.3, 1.3)	8	low A_{HH}
VIII	$2\pi/64, \pi/38$	(0.5, 0.5)	(0.3, 1.3)	8	low A_{HH}
X	$2\pi/64, \pi/38$	(2.5, 0.5)	(0.3, 1.3)	8	high wind
XI	$2\pi/64, \pi/38$	(2.5, 0.5)	(0.3, 1.3)	8	low wind
XII	$2\pi/64, \pi/38$	(2.5, 0.5)	(0.3, 1.3)	8	high A_{MV}
XIII	$2\pi/64, \pi/38$	(2.5, 0.5)	(0.1, 1.3)	8	low A_{HV}

Parameters η_S and η_B are the values of A_{HV} near the surface and below the thermocline, respectively. A_S and A_B are the corresponding surface and deep values of A_{HH}.

Equations (1) and (2) are the equation of horizontal motion and the hydrostatic approximation, respectively. Horizontal bars over all variables are assumed. A_{MV} represents the coefficient of vertical viscosity, and F is a body force representing smaller-scale exchange in the horizontal plane. A complete list of symbols is given in the notation list.

Schemes for approximating the effects of synoptic scale eddies on the ocean circulation have been proposed by Green [1970] and Welander [1973], based on the idea that potential vorticity is approximately conserved. As pointed out in the introduction, these ideas have not been completely worked out and tested in the field or laboratory, so it seems more appropriate for a global ocean model that is to be used in climate studies to use simpler, conventional closure schemes. More elaborate closure schemes for momentum transfer can be introduced at a later stage. Simple mixing of momentum on a sphere gives

$$F^\lambda = A_{MH}\left[\nabla^2 u + (1 - \tan^2\phi)u/a^2 - \frac{2\tan\phi}{\cos\phi a^2}\partial_\lambda v\right] \quad (3)$$

$$F^\phi = A_{MH}\left[\nabla^2 v + (1 - \tan^2\phi)v^2/a^2 + \frac{2\tan\phi}{\cos\phi a^2}\partial_\lambda u\right] \quad (4)$$

The equation of continuity and the equation of state are

$$\partial_z w + \nabla \cdot \mathbf{v} = 0 \quad (5)$$

$$\rho = \rho(\theta, S, p) \quad (6)$$

Density is a complicated function of potential temperature, salinity, and pressure. Polynomial expressions are fitted at

Bottom Topography

Fig. 1. Bathymetry of the high-resolution version of the model based on data of Smith et al. [1966]. Depth is given in kilometers.

standard depths in the model. Details are given by Bryan and Cox [1972].

The conservation equations for potential temperature θ and salt S are

$$\partial_t(\theta, S) + \mathbf{v}\cdot\nabla(\theta, S) + w\partial_z(\theta, S) = \partial_z[A_{HV}\partial_z(\theta, S)]$$
$$+ A_{HH}\nabla^2(\theta, S) \quad (7)$$

Vertical mixing is a function of stability. For $\partial_z\rho < 0$ (the stable case), A_{HV} is taken to be a simple function of the vertical coordinate. In the unstable case it becomes infinite, and temperature and salinity are completely mixed over the unstable parts of the water column. Numerical details are given in the appendix. In addition, the effects of wind stirring on the upper part of the water column are included in the model. At each time step the change in potential energy due to wind stirring is calculated. If the change of potential energy implies a deeper mixed layer, a certain fraction of the layer containing the bottom of the calculated mixed layer is mixed with the surface layers above. In the limit of high vertical resolution the method coincides exactly with that of Kraus and Turner [1967].

The model makes use of simple linear closure schemes, with the exception of vertical diffusion which is a function of vertical stability. A motivation for experiments IV–X, listed in Table 1, is to identify those aspects of the closure scheme which have the greatest impact on the final solutions. These tests will provide a set of priorities for improving the closure scheme at a later stage.

The horizontal and vertical viscosity coefficients A_{MH} and A_{MV} are taken to be constant along the λ, ϕ, and z coordinates. Vertical viscosity for most of the experiments is taken to be 10^{-2} m^2/s. In experiment XII it is increased to 10^{-1} m^2/s. The level of horizontal viscosity is determined by the mesh size, as shown by Bryan et al. [1975]. Observations of float tracks measured during the Mid-Ocean Dynamics Experiment [Rhines, 1977] and local eddy numerical simulations [Orlanski and Cox, 1973; Bretherton and Karweit, 1975] both indicate that mesoscale motions have an effective horizontal diffusivity of approximately 10^3 m^2 s^{-1} in the upper ocean, with somewhat lower values at depth. These data fits to a linear closure scheme do not tell us whether the linear scheme is superior to other possible schemes, but they do indicate what an appropriate linear coefficient should be.

In our model, A_{HH} is taken to be a simple function of the vertical coordinate:

$$A_{HH}(z) = A_B + (A_S - A_B)e^{-0.002z} \quad (8)$$

TABLE 2. Relaxation Constant for Surface Boundary Conditions
and Duration of Each Experiment

Experiment	μ^{-1}, days	Duration, yr	Remarks
I	30	520	annual boundary condition
II	20	510	seasonal boundary condition
III	20	50	high resolution
IV	20	27	low A_{MH}
V	20	27	high A_{MH}
VII	20	100	low A_{HH}
VIII	20	88	low A_{HH}
X	20	60	high wind
XI	20	125	low wind
XII	20	125	high A_{MV}
XIII	20	125	low A_{HV}

The scale depth is 500 m. The different levels of A_S and A_B used in the numerical experiments are shown in Table 1. Recent measurements by *Gregg* [1977] show that vertical mixing is lowest within the thermocline and increases below the thermocline. Therefore A_{HV} is assigned just the opposite vertical dependence as A_{HH}, namely,

$$A_{HV}(z) = 10^4 \{0.8 + (1.05/\pi) \ \tan^{-1} [4.5 \times 10^{-3}(z - 2500)]\}$$
$$(9)$$

With the exception of experiment XIII the upper ocean is assigned the value $A_{HH} = 0.3 \times 10^{-4} \ \text{m}^2 \ \text{s}^{-1}$, within the range of values found in a tritium study by *Rooth and Östlund* [1972]. In the deep ocean the vertical mixing is assigned a value $A_{HV}(z) = 1.3 \times 10^{-4} \ \text{m}^2 \ \text{s}^{-1}$, based on profile estimates by *Munk* [1966].

The high-resolution version of the bottom topography is shown in Figure 1. The topography has been taken from a compilation by *Smith et al.* [1966]. It turns out that details of the bottom topography are quite important for the pattern of deep circulation and for the total transport in the Antarctic Circumpolar Current (ACC). Unfortunately, any large-scale representation is bound to eliminate some features, such as narrow cuts through ridges. Ultimately, studies modeling bottom flow will require much more detailed compilations of the bottom topography than are presently available.

At the bottom,

$$\partial_z(\theta, S) = 0 \quad \partial_z \mathbf{v} = 0 \quad w = 0, \quad \text{at} \ \ z = -H \quad (10)$$

At the side walls,

$$\partial_\eta(\theta, S) = 0, \quad \mathbf{v} = 0 \quad \text{at} \ \ \mathbf{x} = \Gamma \quad (11)$$

where $\partial_\eta(\ \ )$ is the derivative normal to the boundary and Γ is the lateral position of the boundary at any level. At the upper boundary the vertical flux of heat, salinity, and momentum are specified in the following way:

$$A_{HV}\partial_z\theta = \mu(\theta^* - \theta)$$
$$A_{HV}\partial_z S = \mu(S^* - S) \quad (12)$$

and

$$A_{MV}\partial_z v = \tau^* \quad \text{at} \ z = 0$$
$$w = 0 \quad \text{at} \ z = 0 \quad (13)$$

θ^*, S^*, and τ^* are specified both as functions of position and time of the year; μ is an inverse time scale, specified in Table 2. The boundary condition (12) requires θ in the surface layer to follow the seasonal variations of θ^*, but it does not tie θ to θ^* rigidly. Salinity is handled in the same way. Only the annual

mean and first harmonic of the seasonal variation are included in the boundary values, since higher harmonics are difficult to define from available data. The phase of the seasonal variation of θ^*, S^*, and τ^* is also taken to be uniform over the whole globe; θ^* and S^* are taken from a numerical atlas of hydrographic data by *Levitus and Oort* [1977]. The surface temperature and salinity values are interpolated from all available bathythermograph and hydrographic data taken up to 1974. Parameter τ^* is taken from *Hellerman* [1967].

Charts of the annual mean values of τ^*, θ^*, and S^* are shown in Figure 2. The numerical method is that given by *Bryan* [1969], with modifications as outlined in the appendix made to provide a more rapid convergence of the model to an equilibrium with surface boundary conditions.

It should be noted that in the real ocean the flux of salt through the ocean surface is negligible. The surface salt flux is merely an artifice to simulate the effects of evaporation and precipitation in a model of fixed volume.

3. STRATEGY OF THE NUMERICAL EXPERIMENTS

A series of initial value problems have been solved to determine the equilibrium solutions of the model for the various boundary conditions and to learn how sensitive that equilibrium is to changes in the basic parameters of the model.

ANNUAL MEAN

(a) Wind Stress

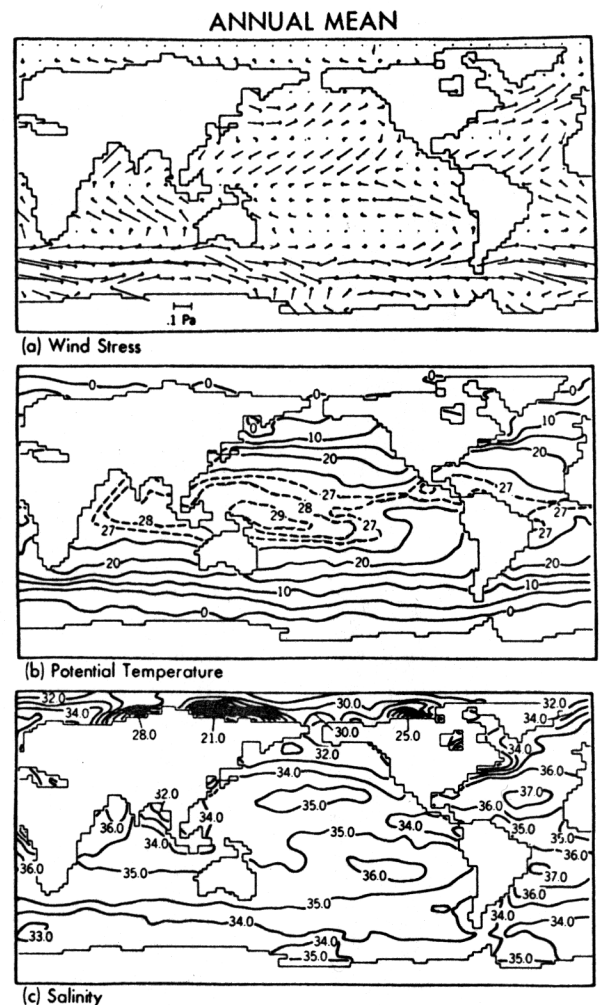(b) Potential Temperature

(c) Salinity

Fig. 2. Annual mean of the boundary conditions imposed at the ocean surface: (a) wind stress from *Hellerman* [1967], (b) surface temperature, and (c) surface salinity from data by *Levitus and Oort* [1977].
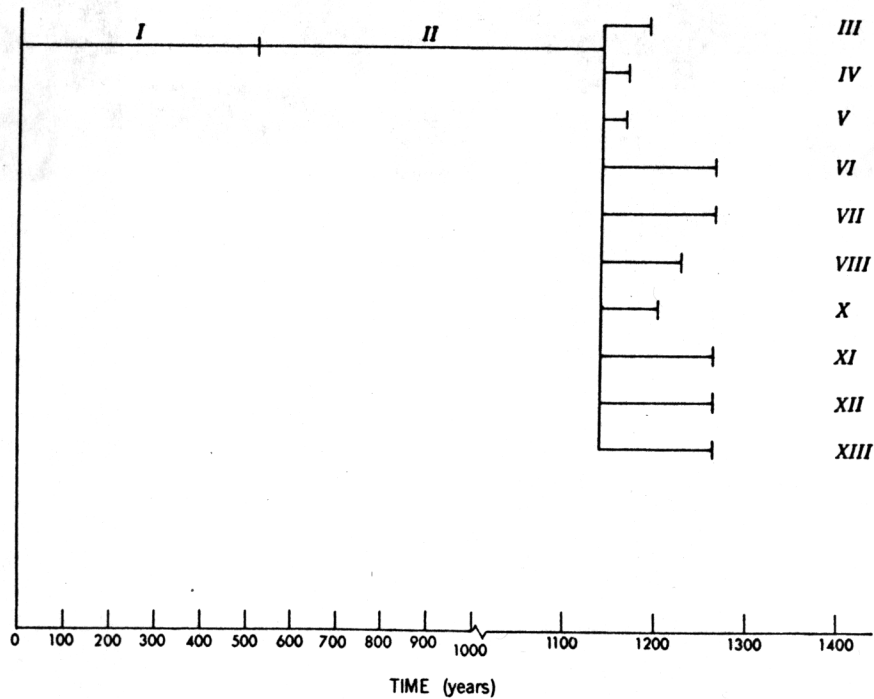
Fig. 3.   Schematic diagram of the numerical experiments. Experiment II is based on initial conditions from experiment I.
Experiments III–XIII are based on initial conditions from experiment II.

Starting with a uniform temperature and salinity for the entire volume of the ocean, boundary conditions without seasonal variations were imposed. This is designated experiment I. The final solution of experiment I is used as the initial conditions for experiment II, in which seasonal variations of surface conditions were imposed. The sequence is shown schematically in Figure 3. The final solution of experiment II is considered a standard case. It formed the initial condition for a whole series of shorter experiments. These experiments were not run out long enough to achieve a steady state, but a careful analysis of the rate of departure of important features, such as overall

thermocline depth, showed the relative importance of the different elements of the closure scheme in the model. Parameter values are shown in Tables 1 and 2.

A picture of the approach to equilibrium in experiments I, II, and III is given in Figure 4. The global average temperature at each level is shown as a function of time; the time scale is appropriate for the upper ocean. At greater depths the time scale was stretched by using a smaller local heat capacity. The details of the method are given in the appendix. Note that equilibrium was achieved quickly near the surface and very slowly at great depth. Experiment I was characterized by a
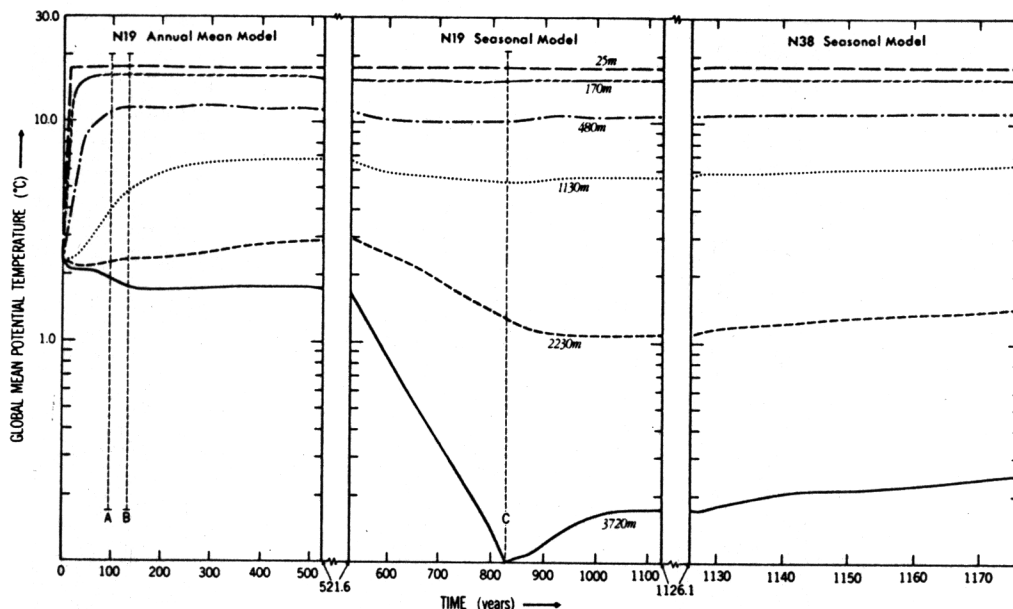

Fig. 4.   Globally averaged temperature as a function of time. Note that the temperature near the surface quickly reaches equilibrium with the surface boundary conditions. At points A, B, and the beginning of the seasonal experiment, the minimum value of $\gamma(z)$ in Table A1 is increased by factors of 2. At point C the surface time constant in Table 2 is reduced to 20 days.
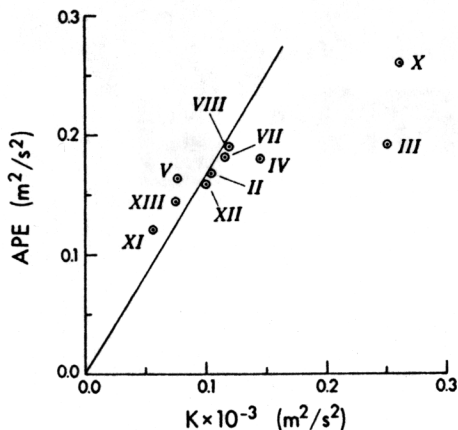
Fig. 5. Available potential energy at the end of each experiment plotted against kinetic energy.

relatively deep thermocline. The thermocline became much shallower in experiment II owing to the large production of cold bottom water in the polar regions.

4. ENERGY RELATIONSHIPS

Many cause and effect relationships in a complicated non-linear system can be understood in terms of energy. An energy analysis turns out to be the best way in which to interpret the effect of varying the closure parameters of the world ocean model. *Holland* [1975] summarizes the energetics of a variety of different numerical models, and his review is an excellent starting point for a discussion of the energy of the general circulation of the ocean.

At the outset it is necessary to derive a few important relationships. If we take a scalar product of $\rho_0 \mathbf{v}$ with the momentum equation (1),

$$\rho_0 \partial_t \mathbf{v}^2/2 = -\nabla[\mathbf{v}(\rho_0 \mathbf{v}^2/2 + p)] - \partial_z[w(\rho_0 \mathbf{v}^2/2 + p)] - g\rho w$$
$$+ \rho_0 \mathbf{v} \cdot F + \partial_z(\rho_0 \mathbf{v} \cdot A_{MV} \partial_z \mathbf{v}) - \rho_0 A_{MV}(\partial_z \mathbf{v})^2 \quad (14)$$

Taking a global average over the entire volume of the world ocean defines an operator,

$$\langle \ \rangle = \frac{1}{\text{volume}} \iiint (\ ) \, dv \quad (15)$$

Applying (15) to (14), we obtain

$$\partial_t K = -\langle g\rho w \rangle + \iint \mathbf{v} \rho_0 \tau a^2 \cos \phi \, d\phi \, d\lambda$$
$$- \langle \rho_0 A_{MH}(\nabla \mathbf{v})^2 + \cdots \rangle - \langle A_{MV}\rho_0(\partial_z \mathbf{v})^2 \rangle \quad (16)$$

where $K = \langle \rho_0 \mathbf{v}^2/2 \rangle$. The change in kinetic energy on the left side of (16) is balanced on the right side by the work done by buoyancy forces, the work done by wind stress, and two dissipative terms. The two negative definite dissipative terms are associated with lateral and vertical friction.

In considering the role of potential energy we depart slightly from *Holland*'s [1975] approach and use the linearized form of available potential energy defined by *Lorenz* [1955]. This form has the advantage that the balance of available potential energy is closely parallel to that of kinetic energy. The linearized form of available potential energy (APE) is defined as

$$\text{APE} = \langle -g\rho'^2/2\partial_z\bar{\rho} \rangle \quad (17)$$

In the sensitivity experiments (III–XIII) we are concerned with rather small departures from near-equilibrium conditions at

the end of experiment II. Therefore we can define the area mean stratification $\partial_z\bar{\rho}$ in (17) on the basis of experiment II without making a large error.

To derive a balance equation for APE, we assume that density obeys the same equation as θ and S in our model:

$$\partial_t\rho + \mathbf{v}\nabla\rho + w\partial_z\rho = A_{HH}\nabla^2\rho + \partial_z(A_{HV}\partial_z\rho) \quad (18)$$

If an overbar defines the area mean, and a prime the departure from the area mean,

$$(\rho, \mathbf{v}, w, A_{HV}) = (\bar{\rho}, \bar{\mathbf{v}}, \bar{w}, \bar{A}_{HV}) + (\rho', \mathbf{v}', w', A_{HV}') \quad (19)$$

Departures of A_{HV} from a horizontal average are due to convective mixing where the stratification is unstable. Substituting (19) in (18) and subtracting the horizontal average, we obtain an equation for $\partial_t\rho'$. Multiplying this equation by ρ' and taking the area mean of the result,

$$\partial_t\overline{\rho'^2}/2 = -\overline{w'\rho'}\,\partial_z\bar{\rho} - A_{HH}\overline{(\nabla\rho')^2}$$
$$- \bar{A}_{HV}\overline{(\partial_z\rho')^2} - \overline{A_{HV}'\partial_z\rho'}\,\partial_z\bar{\rho}$$
$$- \partial_z[\overline{A_{HV}\,\rho'\,\partial_z\rho'} + \overline{\rho'A_{HV}'\,\partial_z\bar{\rho}}]$$
$$+ \text{(higher-order terms)} \quad (20)$$

The higher-order terms omitted in (20) involve triple correlations between deviations from horizontal means. Multiplying (20) by $-g/\partial_z\bar{\rho}$ and applying the global average operator (15),

$$\langle -g\,\partial_t\rho'^2/2\partial_z\bar{\rho} \rangle = \langle g\rho w \rangle + \iint (\rho'B^*/\partial_z\bar{\rho})a^2 \cos\phi\,d\phi\,d\lambda$$
$$+ \langle gA_{HH}\overline{(\nabla\rho')^2}/\partial_z\bar{\rho} \rangle + \langle g\bar{A}_{HV}\overline{(\partial_z\rho')^2}/\partial_z\bar{\rho} \rangle$$
$$+ \langle (g\bar{A}_{HV}\rho'\partial_z\rho' + gA_{HV}'\rho'\partial_z\bar{\rho})\partial_z\partial_z\bar{\rho})/(\partial_z\bar{\rho})^2 \rangle$$
$$+ \text{(higher-order terms)} \quad (21)$$

where B^* represents the surface buoyancy flux. The terms on the right side of (21) can be compared term by term with the right side of the kinetic energy balance equation (16).

The first term on the left side of (21) is the buoyancy work term. The second is the generation of available potential energy by surface buoyancy flux. The surface buoyancy flux is connected with heat and cooling at the surface and differences between rainfall and evaporation. Since $\partial_z\bar{\rho}$ is negative, the next two terms are negative definite. They are parallel to the dissipation terms associated with lateral and vertical friction in the kinetic energy balance. The final term in (21) is an exception. It has no counterpart in the kinetic energy balance. Depending on the mean vertical profile of density, it may be either positive or negative, generating or destroying APE.

Using the energy balance equations (16) and (21) as a guide, it is possible to construct a simpler energy model. If we assume that kinetic energy dissipation is proportional to the kinetic energy itself,
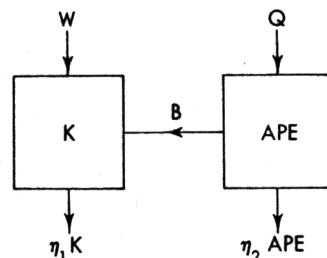

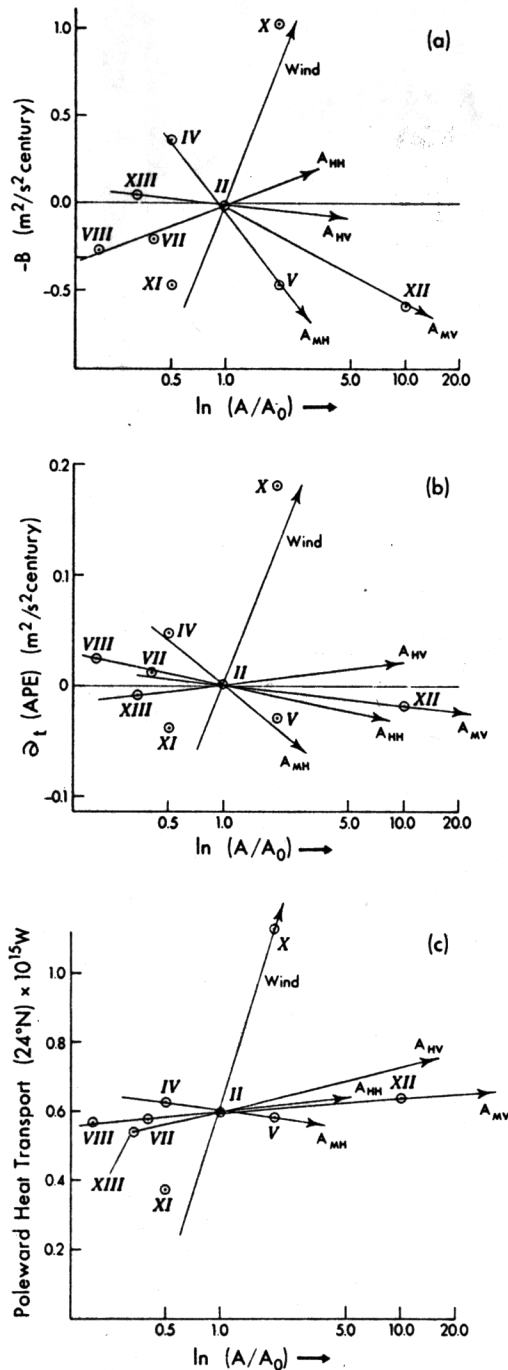Fig. 6. A schematic energy flow diagram.

Fig. 7. Sensitivity diagrams showing the results of parameter variations. A/A_0 is the ratio of a given parameter to its standard value in experiment II: (a) work done by buoyancy forces, (b) change of global available potential energy, and (c) poleward heat transport at 24°N.

$$\partial_t K = B + W - \eta_1 K \qquad (22)$$

B and W are the work done by buoyancy forces and wind, respectively, and η_1 is a constant of proportionality per kinetic energy dissipation. The equivalent equation for APE is

$$\partial_t(\text{APE}) = -B + Q - \eta_2 \text{APE} \qquad (23)$$

Q is the generation term for available potential energy due to surface and subsurface buoyancy flux (the equivalent of the second and fifth terms on the right side of (21)).

Values of APE and K corresponding to all the different experiments are shown in Figure 5. On the scale of the ocean

circulation the available potential energy is many times larger than the kinetic energy, as noted by *Stommel* [1965]. If all driving forces such as wind and differential heating were suddenly switched off, a residual ocean circulation would remain for many years until the available potential energy is exhausted. For most of our experiments, APE and K are approximately proportional to one another. Conspicuous exceptions are experiments III and X. Experiment III is the high-resolution case. Since kinetic energy is associated with narrow swift currents and the largest fraction of available potential energy is in large-scale displacements of the thermocline, it is not difficult to see that higher resolution will allow a larger fraction of the total energy to be in kinetic energy. In the remaining experiments, with the exception of experiment X, geostrophic balance appears to keep the ratio of APE and K approximately the same. In most cases the kinetic energy is associated with baroclinic currents. Any increase in the variance of density causes a corresponding increase in the global kinetic energy.

The simple model given by (22) and (23) is illustrated schematically in Figure 6. *Holland* [1975] pointed out that the sign of B in the numerical models of the ocean circulation that he considered is very dependent on the closure parameters. If the lateral boundary layer governed by A_{MH} was wider than that governed by A_{HH}, B would be positive, and vice versa. This is equivalent to adjusting η_1 or η_2 in Figure 6. A large η_1 will cause energy to flow from APE to K, and the reverse process will occur if η_2 is increased. Apparently, the work done by buoyancy forces adjusts itself to maintain geostrophic balance, which is equivalent to maintaining the nearly constant ratio between APE and K, shown in Figure 5.

The tendency for B to adjust to the closure parameters is illustrated in Figure 7a. The ordinate is $-B$. The abscissa is the logarithm of the ratio of a given parameter to its standard value in experiment II. This method allows us to show the effect of variation of the four mixing parameters and overall wind strength in one graph. The slope of the arrows indicates the degree of sensitivity of the results to a given parameter. Changes in wind are certainly the most important. As seen in the diagram of Figure 5, wind input puts energy directly into kinetic energy. To maintain geostrophic adjustment, energy must flow into APE.

As *Holland* [1975] concluded from earlier experiments, the effects of increasing A_{HH} and increasing A_{MH} on the B term are opposite. Increasing A_{MV} (vertical friction) has the same effect as increasing lateral friction, since it causes the overall dissipation of kinetic energy to increase. One might anticipate that increasing vertical diffusion would have the opposite effect of increasing vertical friction, but this is not the case. The
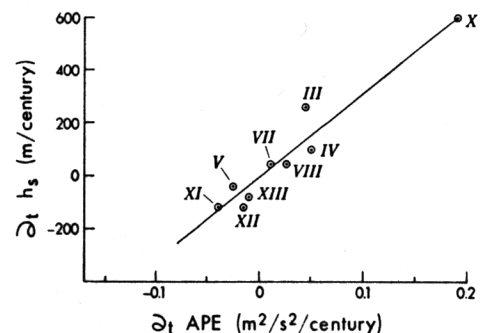

Fig. 8. Tendency of the scale depth of the thermocline versus the tendency of the global available potential energy.
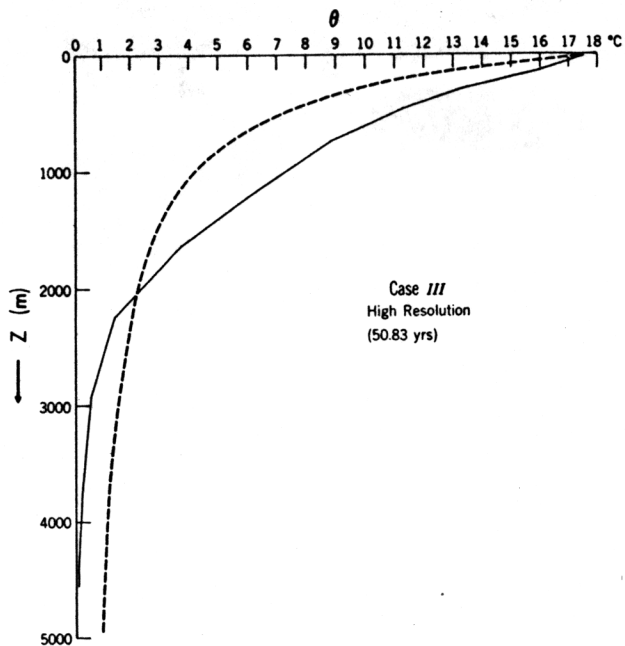
Fig. 9a. Globally averaged potential temperature for experiment III: solid line, calculations; dashed line, observations.

reason for this is the asymmetry between (16) and (21), pointed out earlier. A_{HV} is associated with both a dissipative term and a generation term on the right side of (21). Apparently, the range of parameters is such that an increase in A_{HV} means increased production of APE and a consequent flow of energy from APE to K via the buoyancy term.

The same effects can be seen in the change of APE associated with parameter variations. In Figure 7b the ordinate is the time change of available potential energy. Since the kinetic and available potential energy are nearly proportional to each other over the range of our numerical experiments, we can think of the ordinate as a measure of total energy of the large-scale ocean circulation. The increase in mixing coefficients
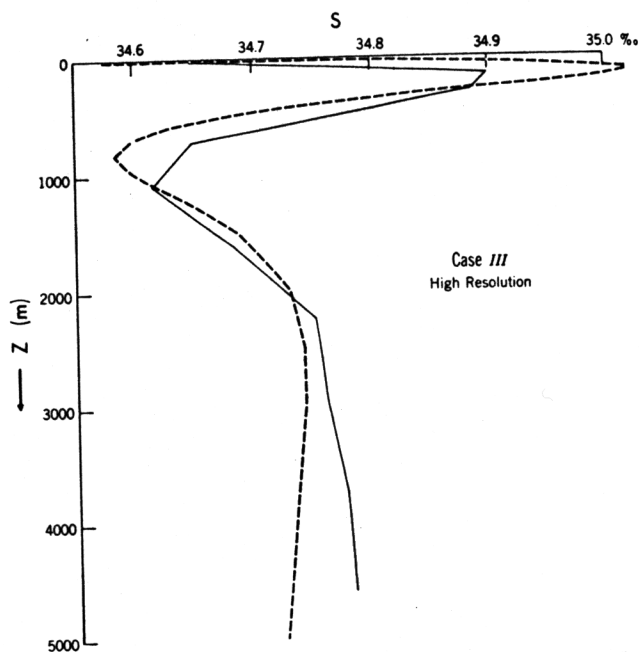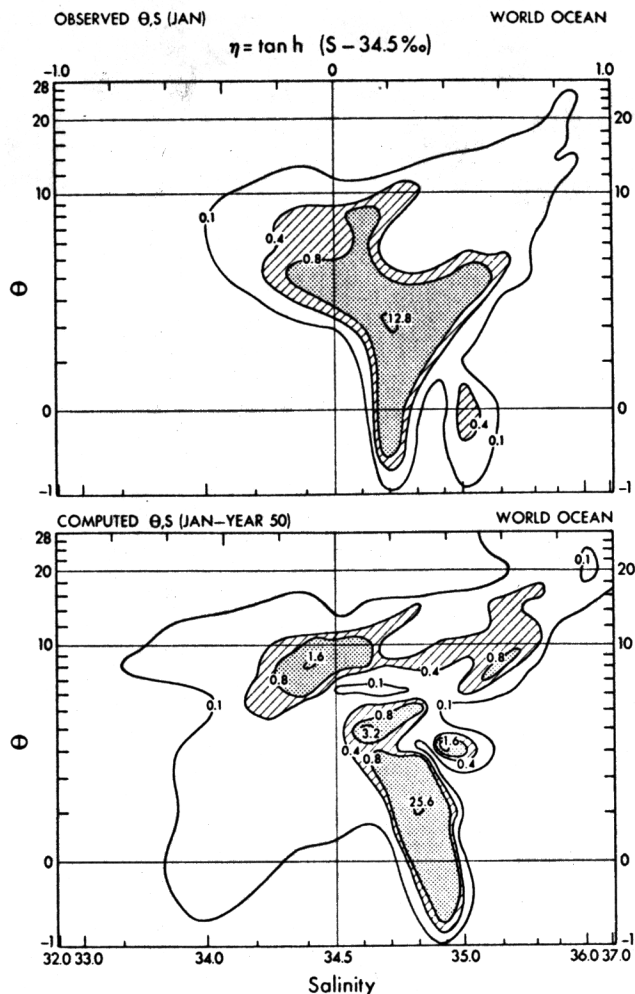

Fig. 9c. Two-dimensional frequency diagram showing water mass characteristics of the world ocean. Units are the percentage volume in each of the categories of Table 3.

Fig. 9b. Same as Figure 9a for salinity.

TABLE 3. Potential Temperature and Salinity Intervals Used to Construct the Water Mass Frequency Diagram in Figure 9c

$\Delta\theta$	ΔS
∞–28.0	∞–37.0
28.0–24.0	37.0–36.0
24.0–20.0	36.0–35.8
20.0–18.0	35.8–35.6
18.0–16.0	35.6–35.4
16.0–14.0	35.4–35.2
14.0–12.0	35.2–35.0
12.0–10.0	35.0–34.9
10.0–8.0	34.9–34.8
8.0–6.0	34.8–34.7
6.0–5.0	34.7–34.6
5.0–4.0	34.6–34.5
4.0–3.0	34.5–34.4
3.0–2.0	34.4–34.2
2.0–1.0	34.2–34.0
1.0–0.0	34.0–33.5
0.0–−1.0	33.5–33.0
−1.0–−2.0	33.0–32.0
−2.0–−∞	32.0–00.0

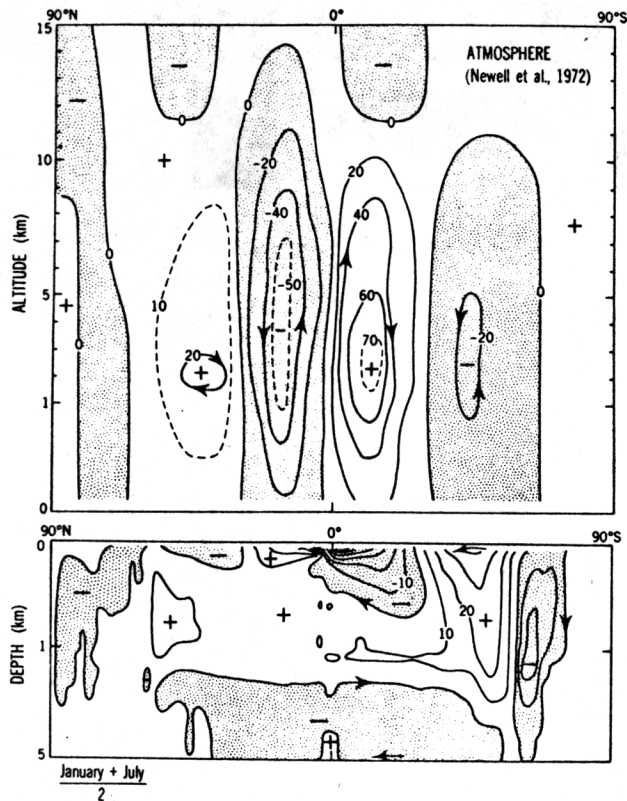Units in Figure 9c are the percentage of the total volume in each of the 19 × 19 water mass intervals defined above.

Fig. 10a. Zonally integrated meridional mass transport in units of 10^6 tons/s (10^9 kg/s. (Top) Observed annual pattern for the atmosphere from *Newell et al.* [1972] and (bottom) model results for experiment III.

related to negative definite terms in the kinetic and available potential energy balances leads to a decrease in total energy. Likewise, an increase in the wind factor leads to an increase of wind work and total energy.

Temperature profiles based on area averages for the model can be fitted by two exponential curves, one for the upper ocean and one for the deep water. The scale depth based on the upper curve is a good measure of thermocline thickness. The upper scale depth is quite sensitive to the parameter variations in our experiments. Figure 8 shows that the scale depth and available potential energy change in a parallel way. Any increase in available potential energy is accompanied by a lowering of the center of gravity for the entire volume of fluid. As long as nonadiabatic processes fix low values of density at the surface in polar regions, horizontal and vertical variations of density must be closely related. The thermocline cannot become thicker without increasing the variance of density within horizontal surfaces, and vice versa. This relationship between the energy of the ocean circulation and the mean thickness of the thermocline is an important relationship which has not been pointed out in previous studies with continuously stratified models.

Finally, we consider the relationship between poleward heat transport and the closure parameters. The poleward heat transport at 24°N is the ordinate in Figure 7c. The abscissa is the same as that of Figure 7a and Figure 7b. Surprisingly, heat transport is not very sensitive to the mixing parameters in the range we are considering. This is a very positive result for the application of this model to climate studies. The effect of wind is much greater, and a possible explanation of this effect in terms of the meridional circulation induced by wind will be

given later in section 6, in which mechanisms of heat transport are analyzed in detail for experiment III.

Our analysis of parameter variations, energy, and thermocline thickness leads to some interesting conclusions with respect to the design of simple climate models of the ocean. For example, it may be desirable to make lateral mixing of heat and momentum small to allow advection to play as large a role as possible. However, this will lead to an unrealistically thick thermocline in the model unless compensating adjustments are made in other parameters to increase the dissipation of energy. In a similar way any increase or decrease of the overall wind work must be compensated by changes in other parameters to prevent the available potential energy and the corresponding thermocline thickness from reaching unrealistic values.

5. GLOBAL INTEGRALS OF WATER MASS PROPERTIES

Meridional sections of S and θ and maps of dynamic topography corresponding to experiment III are shown by *Bryan* [1979]. Meridional cross sections of salinity correspond in a qualitiative way to observations. The great tongues of low-salinity intermediate water are present around Antarctica and in the North Pacific. The salinity structure in the North Atlantic associated with the North Atlantic deep water is also reproduced. In this section, attention will be confined to certain globally averaged integrals of water mass properties not discussed by *Bryan* [1979].

Vertical profiles of temperature and salinity averaged over the entire global ocean are shown in Figures 9a and 9b, respectively. The profiles are compared to averaged observations from *Levitus and Oort* [1977]. As pointed out in the previous section, experiments II and III have a very high level of available potential energy and, consequently, a deeper thermocline than observed. In addition, the deep water is 1°–2°C colder than that observed, owing to the manner in which Antarctic deep water is formed in the model. The corresponding salinity profile in Figure 9b shows that the model is able to simulate the minimum which exists at the base of the thermocline as well as a subsurface maximum in the upper thermocline. Just as the model underpredicts the temperature of the deep water, the salinity of deep water is overpredicted.

Another way to compare global water mass properties of the model with observation is to conduct a volume census of water mass properties. Observations are shown in the upper panel of Figure 9c. The ordinate is the logarithm of potential temperature, and the abscissa is a suitable stretched function of salinity which compresses the high and low extremes of the total range. At low temperatures the salinity is narrowly con-
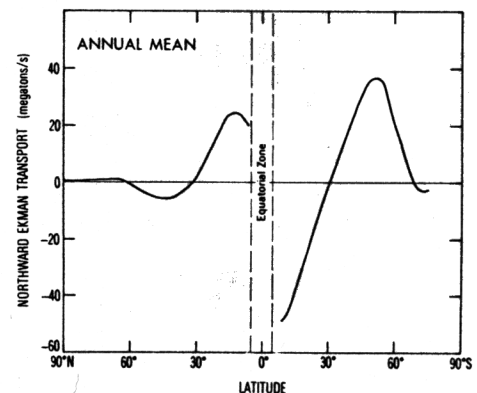

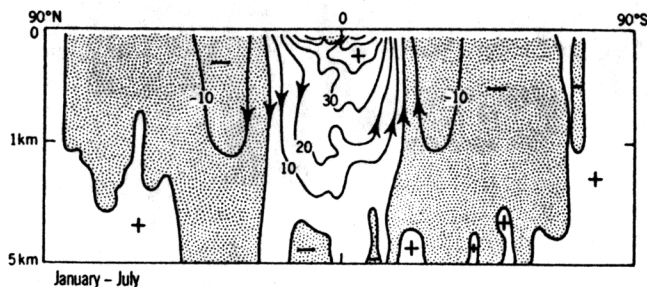Fig. 10b. Annual Ekman transport calculated from *Hellerman*'s [1967] wind stress tables.

Fig. 11. January minus July zonally integrated meridional circulation in units of 10^6 tons/s (10^9 kg/s).

fined, reflecting the fact that the deep waters of the world ocean are rather homogeneous. Higher in the water column, temperature increases, and salinity varies more widely, so that the total pattern looks like an arrowhead pointed downward. A more detailed analysis of individual oceans shows that the extreme high-temperature, high-salinity water is largely in the Atlantic and Indian oceans. The extreme low-salinity water is largely North Pacific and southern ocean intermediate water.

The observed pattern is relatively compact in comparison to the computed water-mass volume census shown in the lower panel for experiment III. The fact that the model thermocline is too deep increases the volume of water around 10°C and decreases the volume of water in the intermediate range of 5°–7°C. The result is a decided gap between thermocline waters and abyssal waters in the model. Note that the volume of water with low temperature and low salinity is much greater in the model. This is due to a slightly thicker halocline than that observed in polar regions.

6. The Circulation in the Meridional Plane

To provide background for a discussion of the poleward heat flux, this section is devoted to a description of the meridional circulation of the model. In the minds of many oceanographers, meridional circulation of the ocean is identified with the thermohaline component. This point of view may be due to the fact that the thermohaline component of the meridional circulation can be most easily identified by tracer methods using the observed fields of temperature, salinity, and oxygen. On the other hand, the model predicts vigorous wind-driven meridional circulations in the upper thermocline. These wind-driven circulations are not easy to detect, since the upper branches are in the surface layer, in which the signatures of water mass properties are rapidly erased by interaction with the atmosphere.

Figure 10a shows the total transport in the meridional plane for experiment III. The circulation is averaged for January and July. In the same figure is the observed annually averaged meridional circulation of the atmosphere according to an observational study by Newell et al. [1972]. The mass transport in the ocean and atmosphere is plotted in the same units (megatons per second; 1 ton equals 10^3 kg). The meridional circulation in the upper thermocline of the ocean tends to be in the same sense (clockwise or counterclockwise) as the atmospheric cell just above it. In the model there is a pair of cells at the equator corresponding to the atmospheric Hadley cells. In addition, there is also a pair of cells at mid-latitudes below the atmospheric Ferrel cells.

Note that the magnitudes of the circulation in terms of mass transport in the ocean and atmosphere are roughly the same. This may be explained by the importance of Ekman transport in the upper ocean and in the atmospheric planetary boundary layer. In these surface layers the Ekman transport in the ocean and atmosphere must correspond approximately in magnitude and be of opposite sign. On a water-covered planet without continents the Ekman transports would be exactly the same across the air-sea interface.

For a quantitative comparison of the cells in Figure 10a the zonally integrated Ekman transport over the ocean is plotted in Figure 10b. A singularity does not allow us to show the total Ekman transport very near the equator. At mid-latitudes there is a strong asymmetry between the hemispheres. The westerlies are stronger in the Southern Hemisphere, and the ratio of ocean to land is greater. Both factors lead to a larger, equatorward Ekman transport in the Southern Hemisphere mid-latitudes relative to that in the Northern Hemisphere mid-latitudes.

Returning to the predicted meridional circulation of the model shown in Figure 10a, we see that the Ekman transport forced by the winds is compensated by return flow in the upper thermocline near the equator. Only in the vicinity of the Antarctic Circumpolar Current does the wind-driven cell penetrate right down to the base of the thermocline. In addition to the wind-driven cells there are additional thermohaline-driven cells at high latitudes. In the Northern Hemisphere there is a downward branch at about 60°N. Detailed examination of meridional circulation patterns for each ocean basin (not shown) indicate that this downward branch is in what corresponds to the Norwegian-Greenland Sea in the model. The sinking is associated with deep water which flows into the North Atlantic and into the Arctic basin with an intensity of approximately 10×10^9 kg/s. In the southern ocean, sinking in the vicinity of Antarctica drives a stronger cell with an intensity of about 30×10^9 kg/s. Only about 5×10^9 kg/s actually penetrates out into the rest of the world ocean; the remaining part recirculates near the Antarctic Circumpolar Current.

In the Northern Hemisphere the middle-latitude wind-driven cell and the thermohaline cell tend to cancel each other partially. In physical terms the Ekman flow toward the equator in the westerly zone is partially offset by net poleward flow in the western boundary currents. This cannot happen very easily in the southern ocean because of its different geometry. The wind-driven overturning circulation below the 'roaring forties' and the thermohaline circulation near Antarctica are physically separated and proportionally much stronger than their Northern Hemisphere counterparts.

A surprising picture emerges if the July meridional transport pattern is subtracted from the January pattern, as shown in Figure 11. The difference pattern shows downward flow at mid-latitudes in the winter hemisphere and upward motion at mid-latitudes in the summer hemisphere. This is consistent with increased Ekman pumping in the subtropical gyre of the winter hemisphere and decreased pumping in mid-latitudes of the summer hemisphere. The model shows that waters are drawn across the equator into the winter hemisphere. The increased surface flow is compensated by a nearly uniform flow of deep water in the opposite direction. In the main thermocline, water converges at the equator throughout the year, but the equatorial upwelling is dominantly fed into a northward or southward Ekman drift, depending on season.

To provide a background for understanding the large seasonal variations of the wind-driven meridional circulation, the difference between winter and summer zonally averaged wind stress is plotted in Figure 12. The upper panel shows clearly that both the easterlies and westerlies increase in the winter
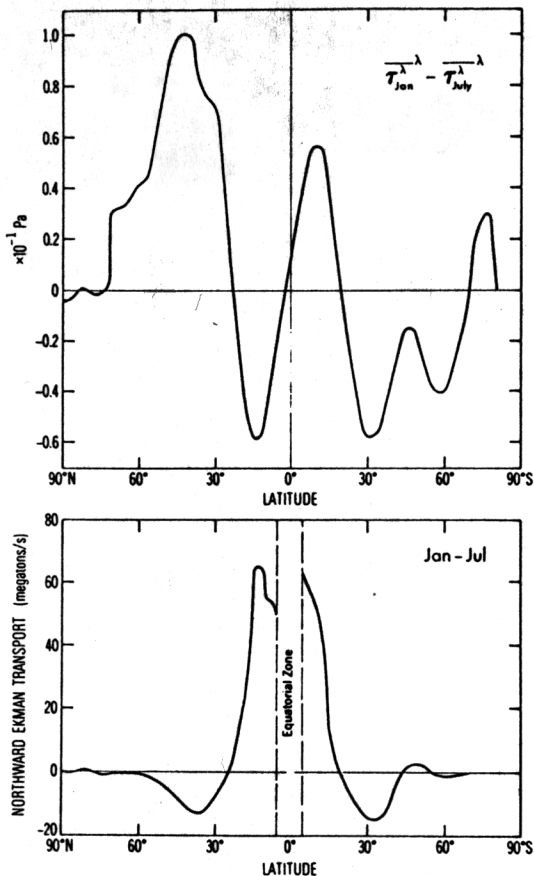
Fig. 12. (Top) January minus July zonally averaged surface wind stress over the oceans in pascals. (Bottom) Corresponding total Ekman transport.

hemisphere. Seasonal variations are less in the Southern Hemisphere as compared to the Northern Hemisphere, owing to the fact that most of the Southern Hemisphere is covered by ocean. The Ekman drift is obtained by dividing the zonally averaged stress by the Coriolis parameter. Winter/summer differences in the zonally averaged wind stress are nonsymmetric across the equator. Since the Coriolis parameter changes sign at the equator, the Ekman transport is approximately symmetric. The main feature is a tendency for a powerful Ekman flux in tropical latitudes toward the winter pole on both sides of the equator. At mid-latitudes the Ekman flux is directed toward the summer pole, accounting for the meridional circulation shown in Figure 10.

7. THE POLEWARD TRANSPORT OF HEAT AND SEASONAL HEAT STORAGE IN EXPERIMENT III

One of the most important motivations for learning more about the general circulation of the ocean is the need to understand the role of the oceans in climate. In this connection the poleward transport of heat by the oceans and the seasonal storage of heat are fundamental. Heat and salinity transport in experiment III have been briefly described by *Bryan* [1979]. In this section the poleward heat transport in the model will be analyzed in more detail to provide some insight into the mechanisms involved. In order to analyze heat transport we define a zonal average as

$$[\ ] = \frac{1}{\Delta\lambda} \int_{\lambda}^{\lambda+\Delta\lambda} (\ ) \, d\lambda \qquad (24)$$

and ( )′ as the departure. The average heat transport across a given latitude may then be written as

$$\{HT\} = \rho c_p \{ \underset{Z}{[v][\theta]} + \underset{G}{[v'\theta']} + \underset{D}{A_{HH} a^{-1} \partial_\phi [\theta]} \} \qquad (25)$$

Z is the component of transport associated with overturning in the meridional plane. Z is only important if zonally averaged currents and zonally averaged temperatures are correlated. G is the transport due to correlations of velocity and temperature at the same level. We may think of this component as being due to correlations in the horizontal plane associated with the major mid-latitude gyres. D is a crude representation of transport by synoptic scale eddies which are only represented implicitly in the model.

Oort and Vonder Haar [1976] have combined heat storage data from the oceans with atmospheric heat balance estimates to calculate the ocean heat transport as a residual term for each month of the year. Their results are shown in Figure 13, accompanied by a similar diagram for the present model. *Oort and Vonder Haar* [1976] also show a strong flux of heat from the Northern Hemisphere to the Southern Hemisphere in summer. A weaker flux in the opposite direction is indicated in April. Maximum poleward flux of heat takes place between 15° and 20° in April and November. The results of experiment III plotted on a similar diagram do not show any indication of two maxima in heat transport. The boundary conditions in wind stress and thermal forcing only contain the first harmonic of the seasonal cycle, and the heat transport responds only to
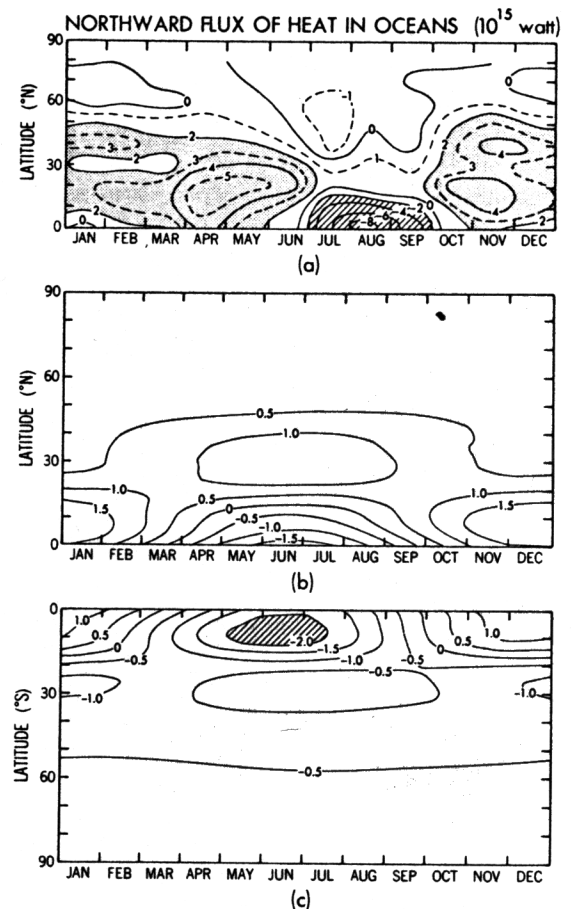

Fig. 13. Northward heat flux by ocean currents as a function of latitude and season. (a) Calculated from atmospheric heat balance by *Oort and Vonder Haar* [1976]. (b and c) Calculated in the model.
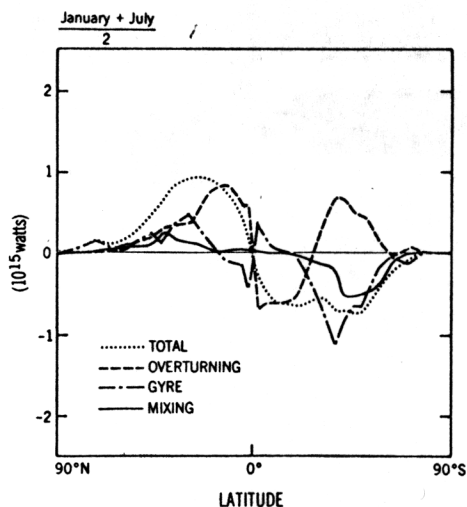
Fig. 14a. January-July average component of poleward heat flux by ocean currents.

the given seasonal forcing. The model indicates maximum poleward transport near the equator in January and a secondary maximum at middle latitudes in July. Quantitatively, the model predicts a maximum heat transport that is only 25% of that given by Oort and Vonder Haar.

The model heat transport in Figure 13 leads the observed by about 1.5 months. This discrepancy is due to the fact that the seasonal boundary conditions on wind and temperature are arbitrarily prescribed in such a way that minimum surface temperature and maximum winds in the Northern Hemisphere occur on January 1. If the phase angle of seasons is prescribed in a more realistic way so that midwinter in the Northern Hemisphere is the middle of February, the discrepancy is removed.

To gain some insight into the mechanism of poleward heat transport in the model, it is necessary to break the heat transport down into the components given in (25). These are shown in Figures 14a and 14b. Looking at the January–July average, we see that the Z component associated with meridional overturning dominates at low latitudes, where heat transport is greatest. Referring to the meridional circulation shown in Figure 10a, we see that a poleward Ekman flux on either side of the equator is compensated by a geostrophic return flow. The upper branch is much warmer than the return flow, resulting in an effective means of transporting heat poleward in both hemispheres.

The dominance of the Z component makes it easy to understand the importance of overall wind strength as shown in Figure 7c. The G component associated with horizontal gyres is most effective at middle latitudes, where east-west temperature differences become greater. It becomes larger at the point where the Z component becomes weaker or, in the case of the Southern Hemisphere, changes sign. The D component is nearly zero at low latitudes and only becomes really important in the vicinity of the large meridional temperature gradients in the ACC. The G component also makes a large contribution in the Southern Hemisphere between 40° and 50°S. More detailed analysis (not shown) indicates that the large contribution of the G component is associated with the configuration of the ACC, which brings relatively warm water southward in the Pacific and returns cold water northward in the Atlantic sector. It is generally thought that the ACC is a barrier to poleward heat transport in the Southern Hemisphere. Figure 14 indicates that this is a somewhat superficial explanation. The

most striking difference between the Northern Hemisphere and the Southern Hemisphere appears to be in the Z component owing to the meridional circulation. Apparently, the very great expanse of ocean under the roaring forties leads to an equatorward Ekman drift that is uncompensated by western boundary currents such as the Gulf Stream or Kuroshio. In Figure 10 the wind-driven cell at mid-latitudes in the Southern Hemisphere is shown to have a strength of over 40×10^9 kg/s. An interesting positive climatic feedback exists here which has not received much attention. Strong westerlies in the atmosphere inhibit poleward heat transport by ocean currents in the Southern Hemisphere, which in turn produces stronger temperature gradients at the sea surface and stronger westerly winds.

The seasonal differences shown in Figure 14b show that the Z component associated with meridional overturning is dominant. If we examine the difference between the January and July meridional circulation shown in Figure 11, we can see that warm surface water carried by the Ekman transport compensated by return flow with the average temperature of the whole water column will explain the details of the seasonal variation of heat transport quite well. The tremendous heat flux from the summer hemisphere to the winter hemisphere requires a surface mass flux of over 40×10^9 kg/s. To obtain a value of 8×10^{15} W, as was indicated in Oort and Vonder Haar's [1976] study by the same mechanism, would require a mass flux of over 100×10^9 kg/s across the equator.

Ocean heat storage moderates seasonal extremes of climate in the same way that poleward heat transport by ocean currents moderates climatic differences between high and low latitudes. The oceans act as an important thermal buffer by storing the excess heat in summer and releasing it the following winter. As an additional check on the usefulness of the model for climate calculations, an analysis has been made of the heat storage in experiment III. For comparison, heat storage computed from bathythermograph observations by Oort and Vonder Haar [1976] has been plotted in Figure 15. Model results for both hemispheres are shown in Figure 16. At mid-latitudes the observed amplitude of the rate of heat storage is about 100 W/m². This may be compared to the size of the solar constant, which is about 1290 W/m². The model predicts 75 W/m² at the same latitude, which is almost within the error range of 10–20 W/m² quoted for the observations by Oort and Vonder Haar

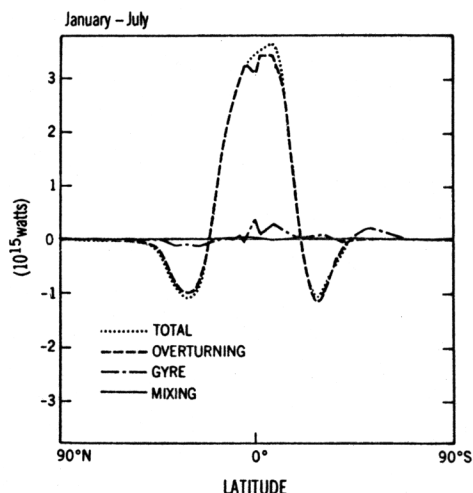Fig. 14b. January minus July component of poleward heat flux by ocean currents.
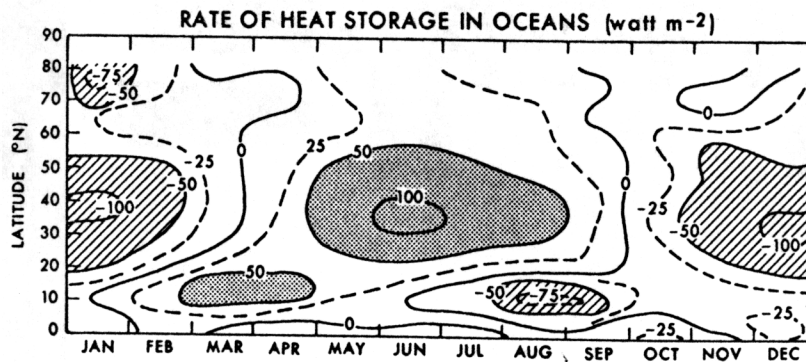
RATE OF HEAT STORAGE IN OCEANS (watt m−2)

Fig. 15. Observed heat storage as a function of latitude and season in the Northern Hemisphere [from *Oort and Vonder Haar*, 1976]. Units are watts per square meter.

[1976]. A more serious discrepancy is the error in phase at mid-latitudes. The model leads the observed rate of heat storage by 1.5 months. As pointed out in connection with Figure 13, this is due to the arbitrary way the seasonal phase is prescribed in the model. It can be removed by specifying that the lowest temperature in the Northern Hemisphere should occur at the sea surface 45 days after the equinox instead of on January 1.

The observed pattern shows an interesting secondary maximum in the tropics which leads the mid-latitude maximum by nearly 3 months. The phase suggests that this pattern is caused by the redistribution of heat by seasonally varying currents rather than by local heating. The boundary conditions and the model itself do not appear to have the resolution needed to simulate this feature.

8. CONCLUSIONS

The ocean circulation is an extremely complex hydrodynamical system which is very difficult to model analytically or in the laboratory. Modern computers, however, have provided a powerful new tool for direct integration of numerical

models which can be used to investigate various processes. In this study we concentrate on the global aspects of the ocean circulation which appear to be very important in determining the earth's climate. A time-dependent model with relatively coarse horizontal resolution (5.63° × 4.74° longitude and latitude, respectively) but relatively detailed vertical resolution (100 m in the upper ocean and 1000 m below) has been numerically integrated over a period equivalent to 1000 years. The time scale has been lengthened in the deep water so that the period of adjustment allowed for is equivalent to more than 2000 years. Climatological values of wind stress, temperature, and salinity are specified at the upper surface as a function of season. Starting with a uniform value of temperature and salinity throughout the entire volume of the world ocean, temperature and salinity structures are allowed to evolve in response to the boundary conditions.

Parameter tests have been carried out to determine the effects of the closure scheme representing unresolved oceanic processes on the large-scale circulation. The tests show a close relationship between the global available potential energy of the ocean circulation and the mean scale depth of the upper
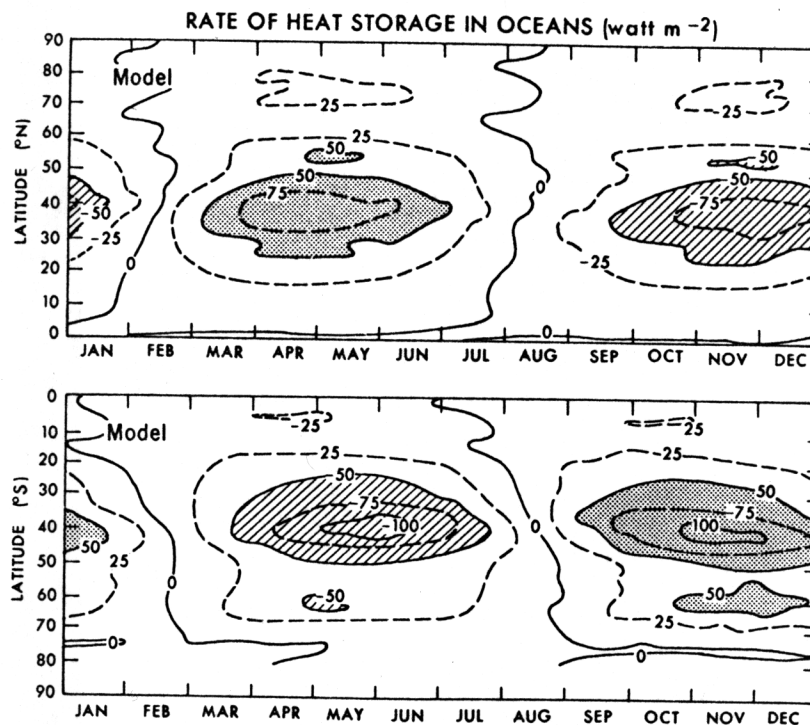
Fig. 16. Same as Figure 15 but calculated by the model in experiment III.

thermocline. Under wide variations of the closure parameters the available potential energy and the total kinetic energy retain a nearly constant ratio. This constant ratio is interpreted as a result of geostrophy. Work done by buoyancy forces transfers energy from the kinetic reservoir to the potential energy reservoir. As noted by *Holland* [1975], the direction of energy transfer by the buoyancy work term is dependent on which reservoir is being depleted faster by the difference between dissipation and energy supplied by wind work and differential heating.

There is a well-defined pattern to the response of the scale depth of the thermocline to parameter changes. Increasing the total wind work or decreasing a dissipation term increases the total energy of the world ocean circulation. Greater energy implies greater displacement of density surfaces and a deeper thermocline in the model. For example, the decrease of lateral mixing of heat or momentum will not by itself improve the model simulation of temperature structure. Decreased lateral mixing of heat allows for greater advection effects and more realistic horizontal gradients in regions like the Gulf Stream. On the other hand, unless compensation in vertical friction is made at the same time, any decrease in lateral mixing causes the total energy to become greater and the thermocline to be deeper.

Poleward transport of heat and water across latitude circles by the ocean circulation is an essential part of the global heat and water balance. Heat balance studies using atmospheric data [*Vonder Haar and Oort*, 1973] indicate that the oceans transport roughly the same amount of heat poleward as the atmosphere transports, but the maximum poleward transport by the ocean circulation is in the tropics and subtropics, while the maximum poleward heat transport by the atmosphere is in middle latitudes. Heat transport in the present study, in which the ocean is driven with climatological winds and temperatures at the upper boundary, can be compared with the results of an earlier study of a combined ocean-atmosphere model [*Bryan et al.*, 1975]. In both cases the dominant mechanism for heat transport in the tropics is a shallow meridional cell which carries warm surface water away from the equator and relatively colder water in the main thermocline toward the equator. The Ekman effect drives surface water away from the equator. In mid-latitudes, however, the Ekman effect drives surface waters toward the equator, inhibiting poleward heat transport. Although the Ekman effect is partly offset by boundary currents in mid-latitudes, heat transport poleward by ocean currents in the vicinity of the atmospheric westerlies is much reduced.

In a high-resolution run with horizontal resolution of 2.81° × 2.37° longitude and latitude, respectively, the horizontal mixing of heat is adjusted to a value of 10^3 m²/s in the upper ocean and a somewhat smaller value below. This value is consistent with area mean estimates from eddy-resolving numerical model calculations by *Orlanski and Cox* [1973], *Bretherton and Karweit* [1975], and more recently, *Semtner and Mintz* [1977]. Breakdown of the poleward heat transport into components shows that in the Northern Hemisphere of the model, mixing plays almost no direct role. In the Southern Hemisphere of the model, mixing is very important in the latitude belt of the Antarctic Circumpolar Current.

In the winter hemisphere both easterlies and westerlies become more intense. This effect leads to enhanced Ekman pumping downward in the subtropical gyre of the winter hemisphere. In the summer hemisphere there is a corresponding weakening of the subtropical Ekman pumping. In the model,

seasonal changes in winds lead to a net shift of surface waters from one hemisphere to another across the equator. Averaged around the globe, the velocity of cross-equatorial flow is about 1 cm/s, but the total transport is very large. Our tentative conclusion is that this seasonal change in meridional circulation caused by wind may explain a seaonally varying cross-equatorial flux of heat which appears in recent heat balance calculations by *Oort and Vonder Haar* [1976], although the model indicates a lower value by a factor of 2. Similar results for a seasonally varying heat transport have been obtained from a much simpler climatic model of the ocean by *Lau* [1978] and *Takano et al.* [1973]. The conclusion must remain tentative for the present because our 2.81° longitude by 2.37° latitude model provides only poor resolution of the complicated dynamics that can occur along the equator. In the real ocean the seasonal changes in meridional circulation shown so clearly in our model solutions may be compensated by seasonal changes in boundary currents. Higher-resolution experiments are planned to explore equatorial seasonal effects in more detail.

APPENDIX: METHOD OF MULTITIME SCALES

The focus of the present study is on the equilibrium response of ocean circulation to specified boundary conditions. If we are not interested in the precise details of the evolution of the model ocean from a state of uniform temperature and salinity to a state in which water masses are fully developed, an implicit treatment of the finite difference equations is indicated. However, the solution of implicit systems can be extremely cumbersome. Since the use of long time steps in an implicit formulation distorts the speed of faster-moving waves in any case, we have adopted a shortcut explicit method which directly alters the equations of motion. The governing equations are changed so that external Rossby waves and internal gravity waves are slowed down to a speed compatible with the actual advection of temperature and salinity.

A brief description of the method is given in the appendix of *Bryan et al.* [1975]. The purpose of this appendix is to present some analysis of the method and to describe a new extension suggested by S. Manabe, which accelerates convergence to equilibrium in the abyssal ocean. Let $\bar{v}$ be the vertically averaged velocity and $\hat{v}$ be the departure from the vertical average. The numerical integration is based on a system of equations corresponding to

$$\alpha \partial_t \bar{v} = G(\phi, \lambda) \qquad (A1)$$

$$\beta \partial_t \hat{v} = F(\phi, \lambda, z) \qquad (A2)$$

$$\gamma(z) \partial_t (\theta, s) = H(\phi, \lambda, z), J(\phi, \lambda, z) \qquad (A3)$$

In a detailed calculation of the time-dependent response of the model, α, β, and γ would all be set equal to unity. In applying the multitime-scale method, α, β, and γ are assigned the values shown in Table A1. The greatest distortion of time scale is implied in the α factor. External Rossby waves are slowed down by a factor of 23. To avoid difficulties in the response to seasonal variations in the wind, $G(\phi, \lambda)$ in (A1) only includes the annual average wind effect.

The new feature of the present computation is the variation of $\gamma(z)$ with depth. In effect, a different time scale is assigned to the deeper levels of the model relative to the surface layers. In a steady state the differences in time scale become unimportant. The accuracy of the method depends on the relative simplicity of the final solutions. A high-resolution model con-

TABLE A1. The Time Step and Constants α, β, and γ Defined in (A1)–(A3)

	Low Resolution	High Resolution
Δt, h	48.7	12.2
α, h	23.4	10.9
β, h	8.8	2.7
$\gamma(z)$, m		
25	1.0	1.0
85	1.0	1.0
169	1.0	1.0
295	1.0	1.0
482	1.0	1.0
754	1.0	1.0
1130	1.0	1.0
1622	1.0	1.0
2228	1.0	1.0
2935	0.98	0.98
3721	0.61	0.61
4565	0.40	0.40

In the earlier stages of the low-resolution run, smaller values of $\gamma(z)$ were applied at the lowest levels.

taining mesoscale eddies will be unstable and highly time dependent. Important features of the mean circulation in an eddy-resolving model would be related to rectified flows. In that case the multitime scale approach would not be appropriate.

To analyze the effect of the time scale factors on the speed of Rossby waves and internal gravity waves, we consider a linearized, inviscid model. It is convenient to represent the variables in terms of the vertical normal modes (*Gill and Clarke* [1974] or *Moore and Philander* [1977]):

$$u, v, p/\rho_0 = \sum_{n=0}^{\alpha} (u^n, v^n, p^n)\hat{p}_n(z) \qquad (A4)$$

$\hat{p}_n(z)$ is the nth vertical mode for a given horizontally uniform stratification. The equations of motion may be written in terms of the amplitude of individual vertical modes. For $n > 0$ and γ equal to unity the equivalent of (A2) and (A3) is

$$\beta \partial_t u^n - fv^n + \partial_x p^n = 0 \qquad (A5)$$

$$\beta \partial_t v^n + fu^n + \partial_y p^n = 0 \qquad (A6)$$

$$\partial_t p^n + c_n^2(\partial_x u^n + \partial_y v^n) = 0 \qquad (A7)$$

We have a set of linear governing equations for each vertical mode that is parallel to the free surface equations for a rotating homogeneous fluid.

Let

$$u^n, v^n, p^n \sim \exp[i(kx + \ell y - \omega t)] \qquad (A8)$$

In the case in which f is a constant, u and v can be eliminated to obtain

$$\omega^2 = (f^2/\beta^2) + (c_n^2/\beta) (k^2 + \ell^2) \qquad (A9)$$

A choice of β larger than 1 reduces the frequency of internal gravity waves.

To examine the effect of β on internal Rossby waves, we return to (A5)–(A7) and make the quasi-geostrophic assumption [*Phillips*, 1963]

$$\partial_t[\beta\nabla^2 - (f/c_n)^2]p + (\partial_y f)_0 \partial_x p = 0 \qquad (A10)$$

The corresponding dispersion relation is

$$\omega = \frac{-k(\partial_y f)_0}{\beta(k^2 + \ell^2) + (f/c_n)^2} \qquad (A11)$$

Note that the effect of β is to increase the dispersion and slow down baroclinic Rossby waves. The effect is greatest on very short waves of the scale of the radius of deformation. For long baroclinic Rossby waves, $k^2 + \ell^2$ may be 2 orders of magnitude less than $(f/c_n)^2$. In that case the effect of β is small.

Finally, we consider the variation of γ in (A3) with respect to z. This approximation was suggested by the fact that the natural time scales of the deep ocean are so much longer than those of the upper ocean. The sluggish currents allow a longer time step without a violation of the Courant-Friedrichs-Levy criterion [*Richtmyer and Morton*, 1967]. We take advantage of that fact by changing the time scale with depth. As a steady state is approached, local time derivatives go to zero, and the value of $\gamma(z)$ becomes immaterial. In Table A1, note that $\gamma(z)$ differs from unity only below the 2-km level, well below the layer influenced by seasonal effects.

One aspect of this method requires more explanation. Convective mixing in the model is done implicitly. Even in a steady state the local derivative in the finite difference model will not go to zero because of vertical mixing. At each time step, statically unstable parts of the water column are mixed vertically so that temperature and salinity are conserved. The average value of temperature over the entire unstable region is assigned to each level within the region. Let θ_k' be the predicted temperature before convective adjustment. From (A3) we have

$$\theta_k' - \theta_k^{m+1} = \gamma_k^{-1}\Delta t H_k^m \qquad (A12)$$

where k is the index of vertical level and m is the index of a time level. Let k_1 and k_2 be the extreme upper and lower levels of a convectively unstable region in the water column. With convective adjustment the predicted value of temperature θ^{m+1} will be

$$\theta_k^{m+1} = \sum_{k_1}^{k_2} \gamma_\ell \theta_\ell' \Delta z_\ell \bigg/ \sum_{k_1}^{k_2} \gamma_\ell \Delta z_\ell \qquad (A13)$$

Note that γ_ℓ is a weighting factor.

Combining (A12) and (A13), we have

$$\theta_k^{m+1} = \sum_{k_1}^{k_2} (\theta_\ell^{m-1}\gamma_\ell + \Delta t H_\ell^m)\Delta z_\ell \bigg/ \sum_{k_1}^{k_2} \gamma_\ell \Delta z_\ell \qquad (A14)$$

The formula (A14) shows that as long as the γ_ℓ weighting factor is used in (A13), the steady state solution in which $\theta_k^{m+1} = \theta_k^{m-1}$ will be independent of γ, the desired result.

NOTATION

λ, ϕ, z longitude, latitude, and vertical distance.

t time.

a, Ω radius and angular velocity of the earth.

$\dot{\lambda}$ relative angular velocity due to ocean currents.

$\mathbf{v}, w$ horizontal velocity vector and vertical velocity component.

p, ρ pressure and density.

$\mathbf{F}$ horizontal body force due to Reynolds stresses, equal to $\mathbf{i}F^\lambda + \mathbf{j}F^\phi$.

θ, S potential temperature and salinity.

A_{MH}, A_{MV} horizontal and vertical turbulence viscosity coefficients.

$A_{HH}(z)$ horizontal diffusivity coefficient, where $A_{HH} = A_B + (A_S - A_B)e^{-0.002z}$.

$A_{HV}(z)$ vertical diffusivity coefficient, where $A_{HV} = \eta_S$ as $z \to 0$ and $A_{HV} = \eta_B$ as $z \to -H$.

μ — time constant used to specify surface heat and salt flux.

B^* — surface buoyancy flux due to heating and net precipitation minus evaporation.

B, W, Q — global integrals of the work done by buoyancy forces, wind, and combined external and internal density changes due to turbulent fluxes.

APE, K — available potential energy and kinetic energy.

η_1, η_2 — linear dissipation coefficients for a simple energy model defined by (22) and (23).

α, β, γ — coefficients used to accelerate convergence of the ocean model defined in (A1)–(A3).

f — Coriolis parameter.

c_n — speed of an internal gravity wave corresponding to the nth vertical mode.

REFERENCES

Andreyev, O. A., B. A. Kagan, and L. A. Oganesyan, On the global circulation in a two-layer model, *Okeanologiya, 16,* 5–13, 1976.

Bretherton, F. P., and M. Karweit, Mid-ocean mesoscale modeling, in *Proceedings of Symposium on Numerical Models of Ocean Circulation,* pp. 237–249, National Academy of Science, Washington, D. C., 1975.

Bryan, K., A numerical method for the study of the circulation of the world ocean, *J. Comput. Phys., 4,* 347–376, 1969.

Bryan, K., Models of the world ocean, in *Dynamics of Atmospheres and Oceans,* Elsevier, New York, in press, 1979.

Bryan, K., and M. D. Cox, An approximate equation of state for numerical models of ocean circulation, *J. Phys. Oceanogr., 2,* 510–514, 1972.

Bryan, K., S. Manabe, and R. Pacanowski, A global ocean-atmosphere climate model, II, The ocean circulation, *J. Phys. Oceangr., 5,* 30–46, 1975.

Gill, A. E., and A. J. Clarke, Wind-induced upwelling, coastal currents, and sea-level changes, *Deep Sea Res., 21,* 325–345, 1974.

Green, J. S. A., Transfer properties of the large-scale eddies and the general circulation of the atmosphere, *Quart. J. Roy. Meteorol. Soc., 96,* 157–185, 1970.

Gregg, M. C., Variations in the intensity of small-scale mixing in the main thermocline, *J. Phys. Oceanogr., 7,* 436–454, 1977.

Hellerman, S., An updated estimate of the wind stress on the world ocean, *Mon. Weather Rev., 95,* 593–606, 1967. (See correction, *96,* 63–74, 1968.)

Holland, W. R., Energetics of baroclinic oceans, in *Proceedings of Symposium on Numerical Models of Ocean Circulations,* pp. 168–177, National Academy of Science, Washington, D. C., 1975.

Holland, W. R., Oceanic general circulation models, in *The Sea,* vol. 6, pp. 3–45, John Wiley, New York, 1977.

Kraus, E. B., and J. S. Turner, A one-dimensional model of the seasonal thermocline, II, The general theory and its consequences, *Tellus, 19,* 98–106, 1967.

Lau, K. N. W., Experiment with a simple ocean-atmosphere climate model: The role of the ocean in global climate, *J. Atmos. Sci., 35,* 1144–1163, 1978.

Levitus, S., and A. H. Oort, Global analysis of oceanographic data, *Bull. Amer. Meteorol. Soc., 58,* 1270–1284, 1977.

Lorenz, E. N., Available potential energy and the maintenance of the general circulation, *Tellus, 7,* 157–167, 1955.

Manabe, S., K. Bryan, and M. J. Spelman, A global ocean-atmosphere climate model, I, The atmospheric circulation, *J. Phys. Oceanogr., 5,* 3–29, 1975.

Moore, D., and S. G. H. Philander, Modelling of the tropical oceanic circulation, *The Sea,* vol. 6, pp. 319–361, John Wiley, New York, 1977.

Munk, W. H., Abyssal recipes, *Deep Sea Res., 13,* 707–730, 1966.

Newell, R. E., J. W. Kidson, D. G. Vincent, and G. J. Boer, *The General Circulation of the Tropical Atmosphere,* vol. 1, 258 pp., MIT Press, Cambridge, Mass., 1972.

Oort, A. H., and T. H. Vonder Haar, On the observed annual cycle in the ocean-atmosphere heat balance over the Northern Hemisphere, *J. Phys. Oceanogr., 6,* 781–800, 1976.

Orlanski, I., and M. D. Cox, Baroclinic instability in ocean currents, *Geophys. Fluid Dyn., 4,* 297–332, 1973.

Phillips, N. A., Geostrophic motion, *Rev. Geophys. Space Phys., 1,* 123–176, 1963.

Rhines, P. B., The dynamics of unsteady currents, in *The Sea,* vol. 6, pp. 189–318, John Wiley, New York, 1977.

Richtmyer, R., and K. Morton, *Difference Methods for Initial-Value Problems,* 2nd ed., 405 pp., Interscience, New York, 1967.

Rooth, C. G., and H. G. Östlund, Penetration of tritium into the Atlantic thermocline, *Deep Sea Res., 19,* 481–492, 1972.

Semtner, A. J., and Y. Mintz, Numerical simulation of the Gulf Stream and mid-ocean eddies, *J. Phys. Oceanogr., 7,* 208–230, 1977.

Smith, S. M., W. H. Menard, and G. Sharman, World-wide ocean depths and continental elevations averaged for areas approximating one-degree squares of latitude and longitude, *Ref. 65-80,* 14 pp., Scripps Inst. of Oceanogr., La Jolla, Calif., 1966.

Stommel, H., *The Gulf Stream, A Physical and Dynamical Description,* 2nd ed., 248 pp., University of California Press, Berkeley, 1965.

Takano, K., Y. Mintz, and Y. Han, Numerical simulation of the world ocean circulation, paper presented at the 2nd Conference on Numerical Prediction, Amer. Meteorol. Soc., Monterey, Calif., 1973.

Veronis, G., Model of world ocean circulation, I, Wind-driven, two-layer, *J. Mar. Res., 31,* 228–288, 1973.

Veronis, G., Model of the world ocean circulation, II, Thermally driven, two-layer, *J. Mar. Res., 34,* 199–216, 1976.

Veronis, G., Use of tracers in circulation studies, in *The Sea,* vol. 6, pp. 169–188, John Wiley, New York, 1977.

Vonder Haar, T. H., and A. H. Oort, New estimate of annual poleward energy transport by Northern Hemisphere oceans, *J. Phys. Oceanogr., 3,* 169–172, 1973.

Welander, P., Lateral friction in the oceans as an effect of potential vorticity mixing, *Geophys. Fluid Dyn., 5,* 173–189, 1973.